Biomaterials 33 (2012) 7530–7539

Contents lists available at SciVerse ScienceDirect

Biomaterials

journal homepage: www.elsevier.com/locate/biomaterials

Radiopaque fluorescence-transparent TaO_x decorated upconversion nanophosphors for *in vivo* CT/MR/UCL trimodal imaging

Qingfeng Xiao [a], Wenbo Bu [a,*], Qingguo Ren [b], Shengjian Zhang [c], Huaiyong Xing [a], Feng Chen [a], Ming Li [b], Xiangpeng Zheng [b], Yanqing Hua [b], Liangping Zhou [c], Weijun Peng [c], Haiyun Qu [a], Zheng Wang [a], Kuaile Zhao [c], Jianlin Shi [a,*]

[a] State Key Laboratory of High Performance Ceramics and Superfine Microstructures, Shanghai Institute of Ceramics, Chinese Academy of Sciences, 1295 Ding-xi Road, Shanghai 200050, PR China
[b] Department of Radiation Oncology, Shanghai Huadong Hospital, Fudan University, Shanghai 200040, PR China
[c] Department of Radiology, Shanghai Cancer Hospital, Fudan University, Shanghai 200032, PR China

ARTICLE INFO

Article history:
Received 10 May 2012
Accepted 16 June 2012
Available online 26 July 2012

Keywords:
Tantalum oxide
Upconversion luminescence
CT
Magnetic resonance
Trimodal imaging

ABSTRACT

To address the intractable issues such as the low performance or biocompatibility frequently encountered in previous CT, magnetic resonance (MR) and fluorescence trimodal imaging nanoprobes, a nanocomposite has been constructed by decorating gadolinium ions doped upconversion nanoparticle (Gd-doped UCNP) with radiopaque but fluorescence-transparent tantalum oxide (TaO_x, $x \approx 1$). The as-synthesized water-soluble nanoparticle showed a litchi-like shape with an average size of ~30 nm and demonstrated extraordinarily high longitudinal and transverse relaxivity values ($r_1 = 11.45\ mM^{-1}s^{-1}$ and $r_2 = 147.3\ mM^{-1}s^{-1}$) compared with the reported Gd-doped UCNPs to date. Obvious CT contrast enhancement was obtained by the combined effect between the radiopaque TaO_x shell and the Gd-doped UCNP inner core. Strong upconversion luminescence (UCL) signal could unobstructedly penetrate out in virtue of high transparency of the TaO_x shell. No mutual interference among different modalities of the upconversion nanolitchi (UCNL) was found, which ensured that the individual merits of every imaging modality could be brought into full play, demonstrated by *in vitro* and *in vivo* imagings. Furthermore, UCNLs showed only a slight effect on macrophages and RBCs *in vitro* and tissue *in vivo*.

1. Introduction

X-ray computed tomography (CT) has been widely used as a medical imaging modality since it could provide three-dimensional (3D) tomography of the anatomic structure based on the differential X-ray absorptions between the tissues and lesions [1]. Currently, small iodinated molecules are the most used clinical CT contrast agents mainly due to their cost-effectiveness rather than contrast performance. Therefore, a distinguishable CT contrast image can only be obtained under a large dosage of iodinated compounds, which may cause potential serious renal toxicity [2,3]. Moreover, the quick renal clearance of iodinated agents would lead to a very short imaging duration, which may result in the difficulty in the target-specific imaging and even the fatal misdiagnosis in clinical applications. Considering these drawbacks of iodinated compounds, recently, utilizing nanoparticles with high atomic number (high-Z) metal elements as potential CT contrast agents to overcome the aforementioned gaps has advanced rapidly. For instance, nanoparticulate Bi_2S_3, TaO_x ($x \approx 1$), Au, Pt, $NaGdF_4$, $NaYbF_4$ and $NaLuF_4$ were well explored as new CT contrast agents and showed obvious CT contrast effect *in vivo* [4–15]. Among them, tantalum oxide with relatively high X-ray attenuation coefficient has recently been given more and more attention due to its excellent biocompatibility referred to as the most important premise for clinical applications. In fact, tantalum and tantalum oxide have been widely employed in clinical tissue engineering as a part of implants or artificial joints [16–18].

Nevertheless, even if highly efficient CT agents were employed, the low detection sensitivity and poor resolution for soft tissue still remained as the inherent shortcomings of CT technology. To solve these sticky problems, apart from the continuous pursuing for the careful modulation of the inherent instrument parameters and exploring more prominent CT contrast agents, integration with other imaging modalities could be the other attractive strategy. For example, optical and magnetic resonance imaging (MRI) modalities are characterized by high sensitivity and good discrimination for

* Corresponding authors. Tel.: +86 21 52412714; fax: +86 21 52413122.
E-mail addresses: wbbu@mail.sic.ac.cn (W. Bu), jlshi@sunm.shcnc.ac.cn (J. Shi).

0142-9612/$ – see front matter © 2012 Elsevier Ltd. All rights reserved.
http://dx.doi.org/10.1016/j.biomaterials.2012.06.028

soft tissues respectively, which could not be achieved with single CT imaging. Therefore, the successful combination of these imaging modalities may result in much more useful information of soft tissues with much enhanced accuracy from cellular to the whole body scales. Previously, Mericle's group fabricated a quantum dot-based nanoprobe (CdS: Mn/ZnS) and demonstrated its capability of CT/MR/optical trimodal imaging, which, unfortunately, suffered from the potential toxicity due to the probable leakage of Cd^{2+} ion. In addition, ultraviolet (UV) light excitation could also cause strong autofluorescence and serious photodamage to tissues, which thus greatly impeded its clinical applications [19]. In contrast, upconversion nanoparticles (UCNPs) can be excited by 980 nm near infrared (NIR) light in the "optical transmission window" of the biological tissue (750–1000 nm), and emit strong luminescence signal from the visible to near infrared of deep light penetration, weak autofluorescence and high signal-to-noise ratio preferable for both *in vitro* and *in vivo* imagings [20–23]. Beyond that, another great advantage of UNCP lies in its ability to introduce magnetic resonance performance by doping Gd^{3+} ion which has seven unpaired electrons and could provide high paramagnetic relaxivity [24–27]. Therefore, Gd-doped UCNPs themselves are naturally magnetic/upconversion nanocomposites with excellent magnetic and optical property, which make them ideal building blocks of CT/MRI/UCL trimodal imaging nanoprobes. Previously, our group prepared a Gd-doped UCNP@SiO_2–Au nanocomposite by a facile reverse emulsion strategy for significant CT/MRI/UCL contrast enhancements. However, the large amount of gold (Au) nanoparticles grafted onto the Gd-doped UCNP@SiO_2 surface, originally designed to give rise to outstanding CT contrast effect, inevitably blocked UCL signal emitted from the inner Gd-doped UCNP [28]. Later, $NaYbF_4$: Er^{3+}/Gd^{3+} nanoparticle proposed by Lu's group exhibited an enhanced CT contrast performance and strong UCL emission intensity. However, the longitudinal relaxation rate (r_1) of this nanoprobe in MRI was unfortunately as small as 0.41 $mM^{-1}s^{-1}$, much lower than the clinical Gd-agent (Gd-DTPA, $r_1 = 5.77\ mM^{-1}s^{-1}$), which remained as an important issue for being furthermore employed as a clinical MR contrast agent [13]. Besides, the biocompatibility of the Yb element has not been well known and no comprehensive *in vivo* data are available to date. Therefore, how to construct a satisfactory CT/MR/UCL trimodal nanoprobe with excellent biocompatibility and simultaneously without sacrificing their individual merits still remains a great challenge.

In this study, we developed a multifunctional nanoprobe with the inherent magnetic/upconversion nanocrystal ($NaYF_4$:Yb^{3+}/Er^{3+}/Tm^{3+}@$NaGdF_4$) as the core and radiopaque but fluorescence-transparent TaO_x as the shell for efficient CT/MR/UCL trimodal imaging. The nanoprobe exhibits a spherical morphology with very rough surface similar to a litchi (lychee): TaO_x nanoparticles are firmly attached on the surface of the $NaYF_4$:Yb^{3+}/Er^{3+}/Tm^{3+}@$NaGdF_4$ core. Therefore, the whole material is named as upconversion nanolitchi (UCNL). The X-ray attenuation, magnetic and upconversion luminescent properties of UCNL were examined in detail. Furthermore, we investigated the feasibility of UCNL for CT/MRI/UCL trimodal imaging both *in vitro* and *in vivo*. The cytoxicity, hemolysis effect and histological assessment have been also systematically evaluated in this report.

2. Experimental

2.1. Materials

Rare-earth chlorides (99.9%), 1-octadecene (90%) and Igepal CO-520 (NP-5) were purchased from Sigma–Aldrich. Oleic acid (OA), NaOH, NH_4F, CH_3OH and CH_3CH_2OH were obtained from Shanghai Lingfeng Chemical Reagent Co., LTD. $Ta(CH_3CH_2O)_5$ was purchased from Meryer Chemical Technology Co., Ltd. 2-methoxy(polyethyleneoxy) propyltrimethoxysilane (PEG-silane) was obtained from Gelest. Cyclohexane was purchased from Sinopharm Chemical Reagent Co., China. All reagents were of analytical grade and used without any purification. Deionized water was used throughout the experiments.

2.2. Synthesis of trimodal nanoprobes

2.2.1. Preparation of $NaYF_4$: Yb^{3+} (20%)/Er^{3+} (2%)/Tm^{3+} (1%) nanocrystals

$YCl_3 \cdot 6H_2O$ (467.17 mg, 1.54 mmol), $YbCl_3 \cdot 6H_2O$ (154.98 mg), $ErCl_3 \cdot 6H_2O$ (15.27 mg, 0.04 mmol) and $TmCl_3 \cdot 6H_2O$ (7.67 mg, 0.02 mmol) in deionized water were added to a 100 mL flask containing 12 mL oleic acid and 30 mL 1-octadecene. The solution was stirred at room temperature for 1 h. Then the mixture was slowly heated to 120 °C to get rid of water under argon atmosphere and maintained at 156 °C for about 1 h until a homogeneous transparent yellow solution was obtained. The system was then cooled down to room temperature with the flowing of argon. Then 10 mL methanol solution of NH_4F (296.3 mg, 8 mmol) and NaOH (200 mg, 5 mmol) was added and the solution was stirred at room temperature for 2 h. After methanol evaporated, the solution was heated to 290 ~ 300 °C and kept for 1.5 h and then it was cooled down to room temperature. The resulting nanoparticles were precipitated by the addition of 20 mL ethanol and collected by centrifugation. The product was redispersed with 10 mL cyclohexane and precipitated by adding 20 mL ethanol, then collected by centrifugation. After four times' washing, the final product was finally dispersed in 20 mL cyclohexane.

2.2.2. Synthesis of $NaYF_4$: Yb^{3+} (20%)/Er^{3+} (2%)/Tm^{3+} (1%)@$NaGdF_4$ nanoparticles

To epitaxially grow $NaGdF_4$ shell over the pre-prepared $NaYF_4$:Yb^{3+}/Er^{3+}/Tm^{3+} core, $GdCl_3 \cdot 6H_2O$ (11.10 mg, 42 μmol) in deionized water was added to a 100 mL flask containing 12 mL oleic acid and 30 mL 1-octadecene and stirred for 1 h. Same process was introduced to remove water in the system. Then, 2 mmol of pre-prepared $NaYF_4$:Yb^{3+}/Er^{3+}/Tm^{3+} in cyclohexane was added, followed by stirring for 1h before heated to 80 °C to evaporate cyclohexane. After that, 1.25 mL methanol solution of NH_4F (6.24 mg, 0.1685 mmol) and NaOH (4.21 mg, 0.1053 mmol) was added into the system and the mixture was stirred at room temperature for another 2 h. Then, methanol was removed at 80 °C, followed by heating the mixture to 280 ~ 290 °C for 1.5 h under argon atmosphere. Same washing steps were followed after the system was naturally cooled to room temperature. The final products were dispersed in 20 mL cyclohexane.

2.2.3. Synthesis of UCNL nanoparticles

Igepal CO-520 (NP-5, 2.3 g) was mixed with cyclohexane (20 mL). The mixture was stirred for 1 h. After that, as-prepared $NaYF_4$:Yb^{3+}/Er^{3+}/Tm^{3+}@$NaGdF_4$-cyclohexane solution (1.5 ml) was added into the mixture. After stirring for 3 h, NaOH solution (0.06 mL, 75 mM) was added and the mixture was stirred for another 2 h. A Syringe Pump was used to control the adding rate, and the solution (1 mL) composed of $Ta(CH_3CH_2O)_5$ (0.1 mL) and cyclohexane (0.9 mL) was introduced into the system within 30 min. To achieve high monodispersity and biocompatibility, PEG-silane (0.05 mL) was added into the mixture. The system was hermetically kept stirring for 24 h. Then methanol was added to precipitate the product and the nanoparticle was collected by centrifugation. The as-prepared nanoparticle was redispersed in ethanol under ultrasonic treatment, precipitated with excess hexane, and collected by centrifugation. This procedure was repeated for three times to remove excess NP-5. The as-obtained nanoparticles could be well-dispersed in ethanol or deionized water. For the synthesis of $NaYF_4$:Yb^{3+}/Er^{3+}/Tm^{3+}@$NaGdF_4$-PEG nanoparticle, other reagents and reaction conditions were same as explained above except that $Ta(CH_3CH_2O)_5$ was not introduced into the system.

2.3. Characterization

The morphology and Energy-dispersive X-ray analysis (EDX) of the nanocomposite were performed on a JEOL 200CX microscope operated at 200 kV. Scanning electron microscopy (SEM) images were obtained on a field emission JEOL JSM-6700F microscope. X-ray diffraction (XRD) patterns were collected using a Rigaku D/Max-2200 PC X-ray diffractometer with Cu target (40 kV, 40 mA). Fourier transform infrwered spectroscopy (FT-IR) spectra were recorded on a Nicolet 7000-C spectrometer by using pressed KBr tablets. Dynamic light scattering (DLS) was performed on Nano-Zetesizer (Malvern Instruments Ltd). Upconversion luminescence emission spectra were collected on Fluorolog-3 Spectrofluorometer (Jobin Yvon, France), with the excitation of a 450 W xenon lamp and an external 0 ~ 1 W adjustable 980 nm semiconductor laser (Beijing Hi-tech Optoelectronic Co., China). The MR imaging experiments were performed on a 3.0-T clinical MRI instrument (GE Signa 3.0T), and the pulse sequence used was a T_1-weighted FSE-XL/90 sequence with the following parameters: TR/TE = 1000, 2000, 3000, 4000/7.9 ms: field of view [FOV]: 18 cm; matrix: 128 × 128; number of excitations (NEX): 2; slice thickness = 2 mm; space = 0.5 mm; FOV: 18 cm; coil: QUADKNEE. The CT tests were performed on GE discovery CT750 HD, GE Healthcare, with spectral CT scanning mode and 0.625 mm slice thickness, with the following parameters: detector coverage, 20.0 mm; pitch and speed, 0.531:1 and 10.62 mm; gantry rotation time, 0.5 s.

2.4. In vitro cytotoxicity of UCNLs against RAW264.7 cells

RAW264.7 (murine macrophage cell line) cells were grown in Dulbecco's Modified Eagle's Medium (DMEM) supplemented with 10% fetal bovine serum (FBS) and 1% penicillin/streptomycin at 37 °C in a humidified 5% CO_2 atmosphere. The cytotoxicity *in vitro* was measured using 3-(4, 5-dimethylthiazol-2-yl)-2, 15-diphenyltetrazolium bromide (MTT) assay. RAW264.7 cells were seeded into a 96-well cell-culture plate at 10^4/well and then incubated for 24 h at 37 °C under 5% CO_2. DMEM solutions of UCNLs with different concentrations of 0, 15.625, 31.25, 62.5, 125, 250, 500 and 1000 μg/mL were added to the wells. The cells were then incubated for 6 or 24 h at 37 °C under 5% CO_2. Cell viability was determined by MTT assay.

2.5. Hemolysis assay

The experiment was carried out according to previous report [45]. Human blood stabilized by EDTA was kindly provided by Shanghai Blood Center. The red blood cells (RBCs) were obtained by getting rid of the serum from the blood by centrifugation and suction. The cells were diluted to 1/10 of their volume with PBS solution. 0.3 mL diluted RBS suspension was then mixed with: a) 1.2 mL of PBS as a negative control; b) 1.2 mL deionized water as a positive control; c) 1.2 mL UCNL suspensions with different concentrations of 0, 15.625, 31.25, 62.5, 125, 250, 500 and 1000 μg/mL. The mixtures were then vortexed and let to rest for 2 h at room temperature. Then the samples were centrifuged and the absorbance of the supernatants at 541 nm was measured by UV–Vis characterization.

2.6. Cellular uptake

RAW264.7 cells were initially seeded and allowed to adhere for 24 h at 37 °C and 5% CO_2. The cells were incubated in culture medium containing UCNLs (1 mg/mL) for different time (3, 6 and 12 h) at 37 °C and 5% CO_2. Subsequently, the cells were washed with PBS for four times to remove excess nanoparticles. Then, nuclei were stained with 4′-6-Diamidino-2-phenylindole (DAPI) for 15 min. The process of cellular uptake could be monitored with an Olympus FV1000 laser-scanning microscope equipped with a CW NIR laser at 980 nm as the excitation source, while DAPI was excited with 359 nm light. A 60× oil-immersion objective lens was used and luminescence signals were detected in the wavelength regions of 500–560 nm and 620–680 nm.

2.7. Confocal fluorescence imaging in vitro

Medium containing different concentrations of UCNLs (0, 0.5 and 1 mg/mL) was incubated with RAW264.7 cells (10^6/well) for 24 h at 37 °C and 5% CO_2. Subsequently, the cells were washed with PBS for four times to remove excess nanoparticles. Then, fluorescence imaging of cells was acquired with confocal microscopy.

2.8. MR and CT imaging in vitro

RAW264.7 cells were seeded onto culture dishes at a density of 10^6 cells per plate in 10 mL of media for 24 h at 37 °C under 5% CO_2. After washing with PBS for three times, different concentrations of UCNLs dispersion (0, 0.5 and 1 mg/mL) were added. After 24 h, the cells were washed three times with PBS to remove free nanoparticles and detached by the addition of 1 mL of trypsin/EDTA (Gibco). After centrifugation, RAW264.7 cells containing UCNLs in PBS were precipitated at the bottom of the 1.5 mL centrifuge tube. The MR and CT imaging experiments were performed on a 3.0-T clinical MRI and CT instrument, respectively.

2.9. Trimodal CT/UCL/MRI imaging of UCNLs in vivo

Kunming mice with average weight of 20 g were purchased from Laboratory animal center, shanghai medical college of Fudan University. Animal procedures were in agreement with the guidelines of the Regional Ethics Committee for Animal Experiments. Kunming mouse (~20 g) was anesthetized using 10% chloral hydrate (150 μL). Subsequently, UCNL dispersion was injected through the tail vein into the mouse. *In vivo* trimodal imaging was performed at appropriate time points after tail vein injection.

3. Results and discussion

3.1. Characterizations of trimodal nanoprobes

Modified water-in-oil (W/O) reverse microemulsion method (Scheme 1) was used for the fabrication of UCNLs [5]. Firstly, $NaYF_4$:Yb^{3+}/Er^{3+}/Tm^{3+}@$NaGdF_4$ was synthesized by a seed-mediated regrowth method using our previously reported procedures [29]. As indicated in the typical low-magnification transmission electron microscopy (TEM) images (Fig. 1a and b), the as-prepared $NaYF_4$:Yb^{3+}/Er^{3+}/Tm^{3+} and $NaYF_4$:Yb^{3+}/Er^{3+}/Tm^{3+}@$NaGdF_4$ exhibit excellent monodispersity and sharp size distributions with the average diameters of about 26.2 and 26.5 nm, respectively (Fig. S1a and b). No morphological change and undesired heterodimer structures could be observed in the high-magnification TEM image of the $NaYF_4$:Yb^{3+}/Er^{3+}/Tm^{3+}@$NaGdF_4$ nanoparticle, which indicated the successful regrowth of the $NaGdF_4$ shell (Fig. S2a). More detailed structural information obtained from the HR-TEM image shows the presence of (1 0 $\bar{1}$ 0) and (0 1 $\bar{1}$ 0) lattice planes with equal interplanar spacing of

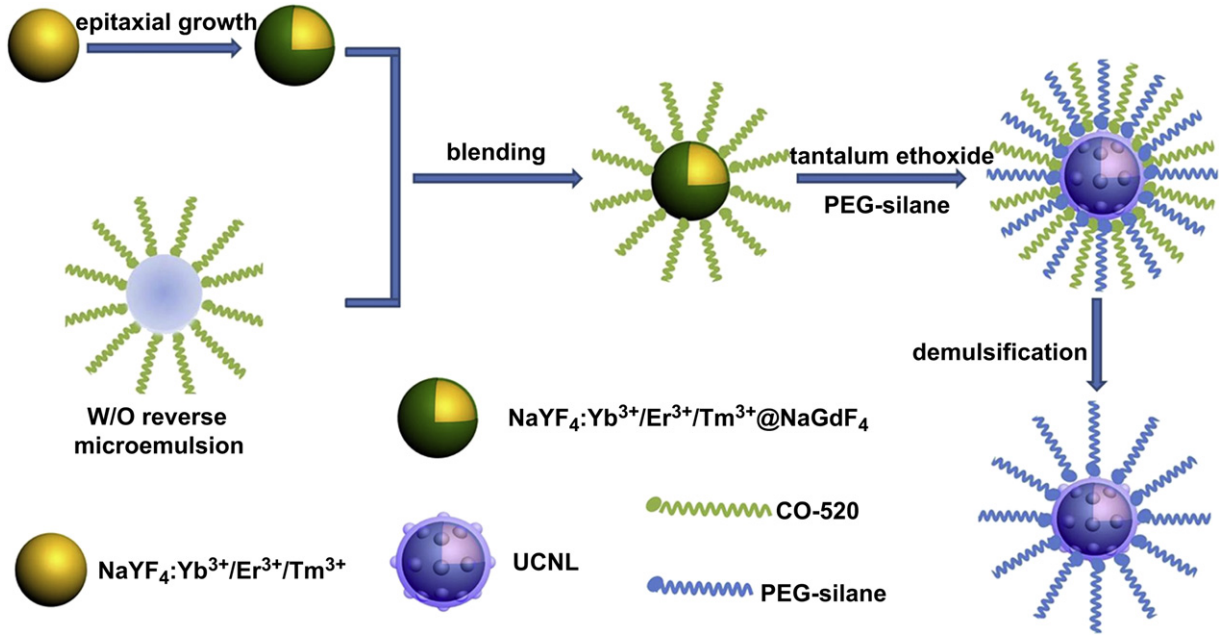

Scheme 1. Schematic illustration of the synthetic procedures of UCNLs with $NaYF_4$:Yb^{3+}/Er^{3+}/Tm^{3+}@$NaGdF_4$ as the core and radiopaque but fluorescence-transparent TaO_x as the shell.

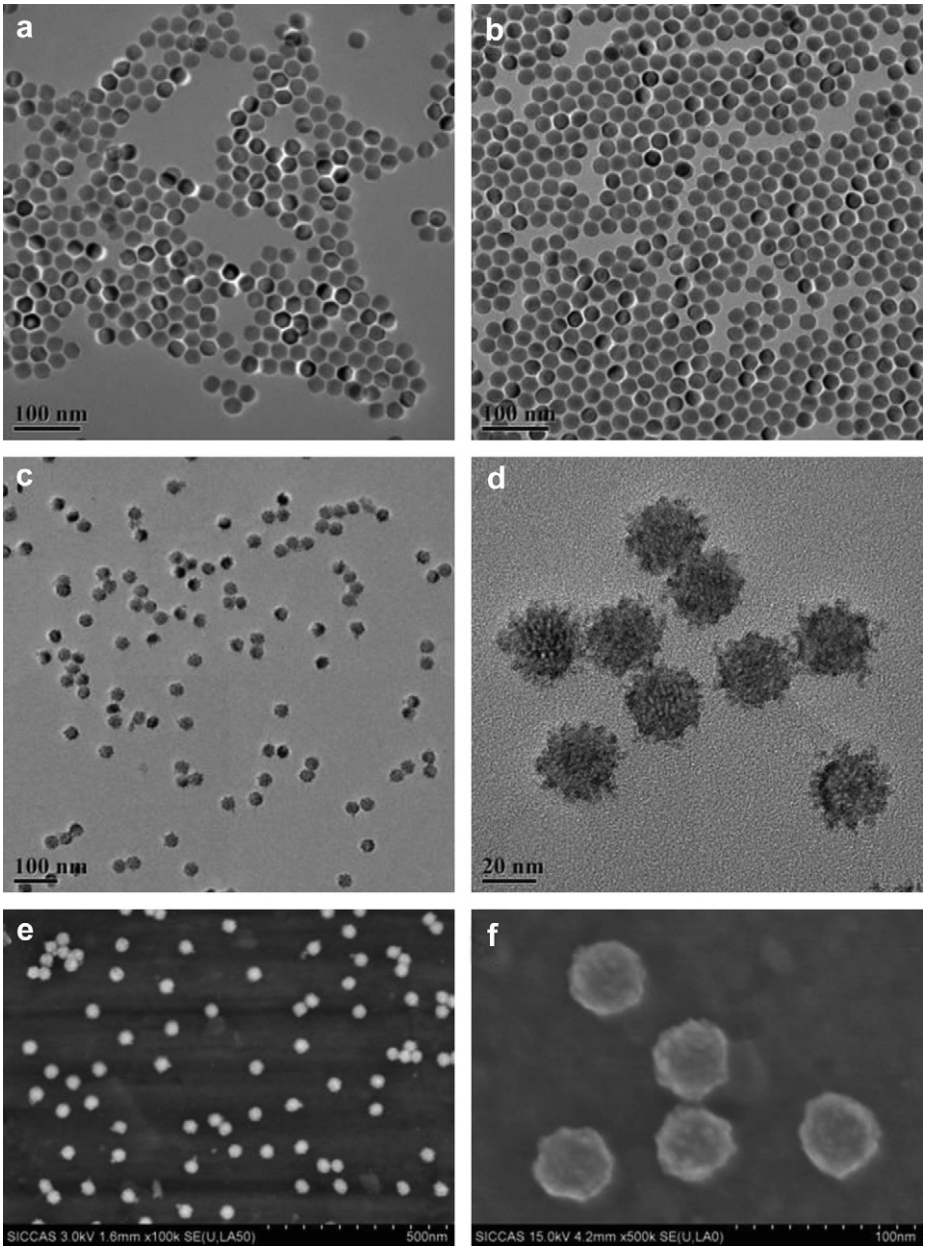

Fig. 1. Low-magnification TEM images of (a) $NaYF_4$:Yb^{3+}/Er^{3+}/Tm^{3+}, (b) $NaYF_4$:Yb^{3+}/Er^{3+}/Tm^{3+} @$NaGdF_4$. TEM (c, d) and SEM (e, f) images of UCNLs at different magnifications.

0.52 nm corresponding to the JCPDS 16-0334 hexagonal structure (Fig. S2b) [25]. The selected area electron diffraction (SAED) pattern further confirmed the exclusive existence of pure hexagonal structure with no detectable cubic phase, which was required for the *in vivo* UCL imaging (Fig. S2c). Secondly, the OA-capped $NaYF_4$:Yb^{3+}/Er^{3+}/Tm^{3+}@$NaGdF_4$ dispersed in cyclohexane was added to the pre-prepared reverse microemulsion system of an Igepal CO-520 and cyclohexane mixture, followed by the injection of tantalum (V) ethoxide. Carefully maintaining the reaction rate of tantalum ethoxide is one of the key elements and tantalum ethoxide should be reasonably diluted with cyclohexane before being added to the system. Later, PEG-silane was introduced to prevent the aggregation among the particles for keeping excellent monodispersity and improving the biocompatibility in the meantime. It is worthy to mention that the TaO_x layer decorated onto the inner core by this method consists of tantalum suboxides ($x \approx 1$) in amorphous phase according to the previous report [5]. Fig. 1c and d shows that the ultrasmall particles are attached over the smooth particle surface, leading to the increase of overall diameter to ~30 nm (*ca.* 3.5 nm-thick TaO_x layer), demonstrating the successful decoration of the TaO_x shell (Fig. S2d). More unambiguous surface morphology could be observed with scanning electron microscope (SEM) (Fig. 1e and f). Dynamic light scattering (DLS) analysis showed that the UCNL had an average hydrodynamic diameter of about 69.3 nm. Compared with the TEM size, the increase of hydrodynamic diameter could be ascribed to the dwelling effect of the outer layer of PEG-silane coating (Fig. S3). Energy dispersive X-ray (EDX) analysis verified the presence of the relevant elements of $NaYF_4$:Yb^{3+}/Er^{3+}/Tm^{3+}, $NaYF_4$:Yb^{3+}/Er^{3+}/Tm^{3+}@$NaGdF_4$ and UCNL (Fig. S4). Consecutive appearance of representative elements, such as Gd and Ta, after the seed-mediated regrowth and decoration procedures indicated the successful coating of $NaGdF_4$ and TaO_x. The X-ray diffraction (XRD) patterns in Fig. S5 demonstrate that both $NaYF_4$:Yb^{3+}/Er^{3+}/Tm^{3+} and $NaYF_4$:Yb^{3+}/Er^{3+}/Tm^{3+}@$NaGdF_4$

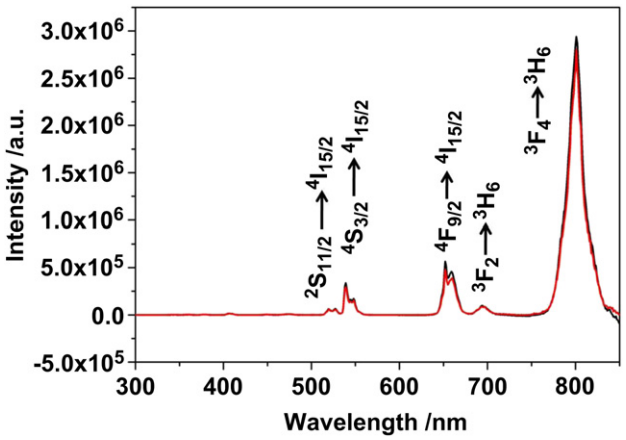

Fig. 2. Room temperature UCL spectra of $NaYF_4$:Yb^{3+}/Er^{3+}/Tm^{3+}@$NaGdF_4$-PEG (black line) and UCNL (red line). (For interpretation of the references to color in this figure legend, the reader is referred to the web version of this article.)

exist in a pure hexagonal phase, consistent with the SAED patterns. However, very rough baseline and a small peak at around 30° appeared after coating TaO_x, which should be attributable to the amorphism of TaO_x shell, in line with the previous report [5]. The successful surface modification was further attested by Fourier transform infrared spectroscopy (FT-IR) (Fig. S6). For hydrophobic oleate capped $NaYF_4$:Yb^{3+}/Er^{3+}/Tm^{3+}@$NaGdF_4$, bands at 1552 and 1459 cm^{-1} were attributable to the asymmetric and symmetric vibration modes of the carboxylic group (C═O); the transmission bands located at 2956 and 2923 cm^{-1} could be assigned to the asymmetric and symmetric stretching vibrations of methylene group (–CH_2) in the long alkyl chain of OA. The 3438 cm^{-1} band was for the stretching vibration of the O–H (COOH); the broad peak at 3126 cm^{-1} could be assigned to the ═C–H stretching vibration [28,30,31]. However, after decorating TaO_x shell, former broad peak at 3126 cm^{-1} disappeared with a new band showing up at 630 cm^{-1} assigned to the symmetric vibration modes of the Ta–O–Ta [32]. These variations of the functional groups in FT-IR spectra are indicative of the successful surface decoration process. To demonstrate the transparency of the TaO_x shell, the upconversion emission spectra of $NaYF_4$:Yb^{3+}/Er^{3+}/Tm^{3+}@$NaGdF_4$-PEG and UCNL in aqueous solution under the same yttrium concentrations (59.2 μg/mL) were compared. Both of them show the sharp emission peaks located at 519 nm ($^2H_{11/2} \rightarrow {}^4I_{15/2}$), 538 nm ($^4S_{3/2} \rightarrow {}^4I_{15/2}$), 652 nm ($^4F_{9/2} \rightarrow {}^4I_{15/2}$) from Er^{3+} and 693 nm ($^3F_2 \rightarrow {}^3H_6$), 800 nm ($^3F_4 \rightarrow {}^3H_6$) corresponding to Tm^{3+}. No significant change of the luminescence intensity at the characteristic emission wavelength (especially 800 nm) can be observed before and after the

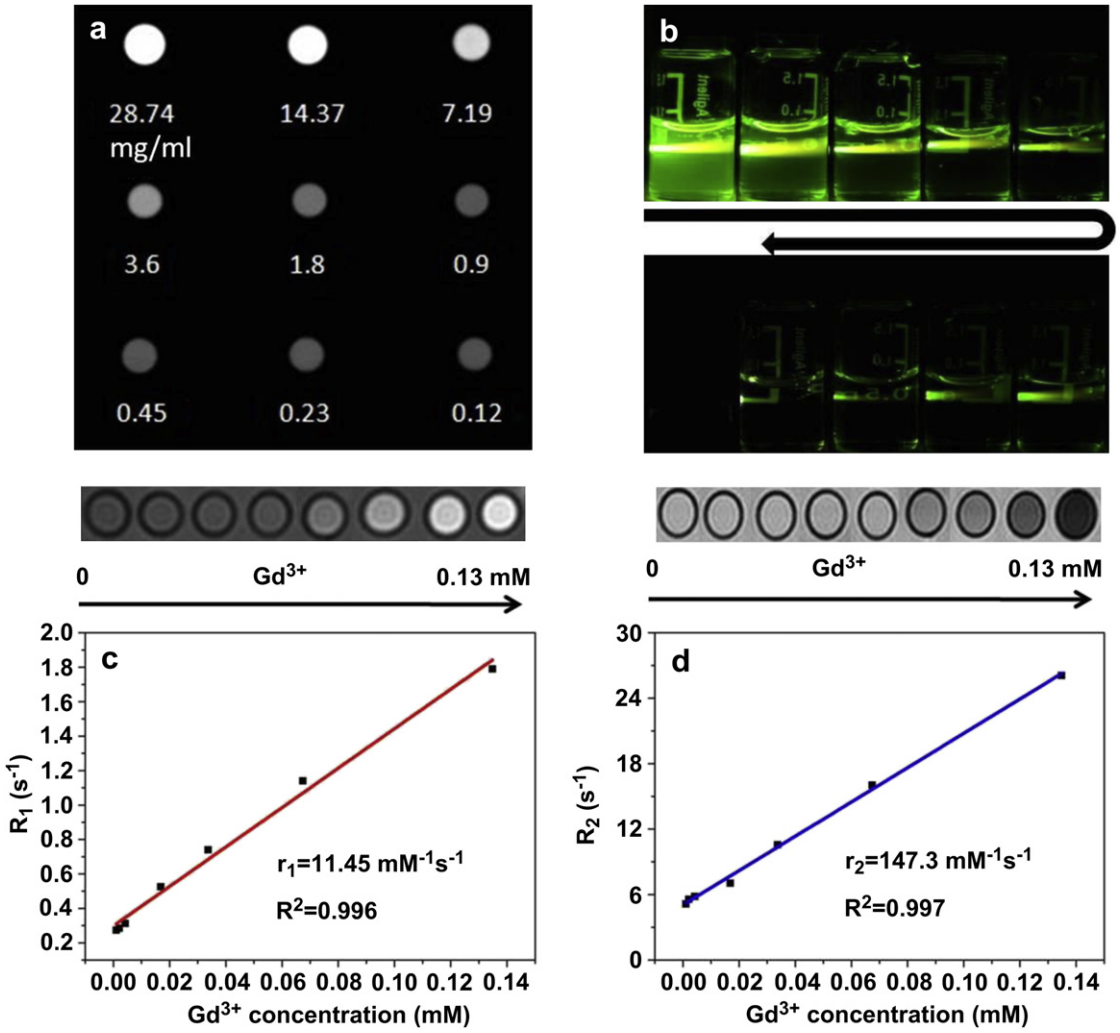

Fig. 3. CT images and the corresponding HU values (a) of UCNLs at varied concentrations, Digital photos (b) of samples under 980 excitation at different concentrations of UCNLs: from 5.2 mg/mL to 0 mg/ml (water) along the direction of the arrow, laser power: 2W. (c) T_1-weighted MR images and relaxation rate R_1 ($1/T_1$) *versus* Gd^{3+}-concentration, (d) T_2-weighted MR images and relaxation rate R_2 ($1/T_2$) *versus* Gd^{3+}-concentration. Deionized water (0 mg/mL) was the reference.

Table 1
Comparison of r_1 and r_2 values (per Gd^{3+} ion) of Gd^{3+}-doped UCNPs between this work and previous literature reports.

Nanoparticles	r_1 ($mM^{-1}s^{-1}$)	r_2 ($mM^{-1}s^{-1}$)	Reference
UCNL	11.45	147.3	This work
β-$NaGdF_4$	7.2	22.7	38
$NaYF_4$:Yb^{3+}/Er^{3+} @ (0.2 nm) $NaGdF_4$	6.18	–	29
$NaYF_4$:Yb^{3+}/Er^{3+} @ (6 nm) $NaGdF_4$	0.48	12.5	37
$NaYF_4$:Yb^{3+}/Er^{3+}/Gd^{3+}	0.14	8.7	36

decoration of TaO_x (Fig. 2), demonstrating that the TaO_x shell is highly transparent to both 980 nm laser and the emitted light from the Gd-doped UCNP core. Therefore, the great reduction of the fluorescence intensity in most previously reported multi-modalities nanoprobes can be effectively avoided in the present UCNL system [28,33]. In addition, it is worth noting that the emission intensity at 800 nm is obviously stronger in comparison to other emissions, which facilitates the following UCL imaging *in vivo* because 800 nm NIR light has deeper tissue penetration than visible light [34].

3.2. Trimodal imaging demonstrations of UCNL in aqueous solution

CT images were acquired using varied concentrations of UCNLs dispersed in deionized water, which displayed notable signal enhancement at the increased concentrations of UCNLs (Fig. 3a). It should be pointed out that in addition to the main contribution by Ta element with a high X-ray attenuation coefficient in promoting CT contrast effect, the auxiliary effect to the signal enhancement from $NaYF_4$:Yb^{3+}/Er^{3+}/Tm^{3+}@$NaGdF_4$ also should not be neglected due to the presence of several rare earth elements (Yb, Er, Tm, Gd), which also contributed in making UCNL an eligible CT contrast agent [35]. UCL images of this nanoprobe obtained under the excitation of a continue wave (CW) laser (λ = 980 nm) exhibit concentration- and power-dependent green-yellow light emissions ascribed to the blending of its typical green with red luminescence (Figs. 3b and S7). T_1 and T_2-weighted MR images of UCNL acquired on a 3.0 T MR scanner reveal the concentration-dependent brightening and darkening effects, presenting the highest r_1 value of 11.45 $mM^{-1}s^{-1}$ and r_2 value of 147.3 $mM^{-1}s^{-1}$ to date among the reported Gd-doped UCNPs (Fig. 3c and d). In fact, great efforts have been made to obtain relatively high r_1 and r_2 values by focusing on designing and tuning the structures (Table 1) [29,36–38]. Herein, the ultrathin $NaGdF_4$ layer was epitaxially grown on the surface of $NaYF_4$:Yb^{3+}/Er^{3+}/Tm^{3+} and most Gd ions should be located on the surface instead of within the crystal lattice, thus effectively suppressing "negative-lattice shield effect" (n-LSE) reported by our group [29], which should be one of the most important reasons for obtaining the maximal r_1 and r_2 values among the reported Gd-doped UCNPs. In addition, it is assumed that in spite of non-intrinsic magnetism, TaO_x shell as an interlayer might to a certain extent affect the interaction process between the inner core and surrounding water molecules and then varied the final r_1 and r_2 values. However, the detailed mechanism remains unclear.

3.3. Cytotoxicity and hemolysis assays of UCNL

Regarding the cytotoxicity of UCNL, Methyl thiazolyl tetrazolium (MTT) assay was conducted using RAW264.7 cells to determine the influence of varied concentrations of UCNLs on the cell viability. As shown in Fig. S8, the cellular viability could maintain at around 90% after 6 h of incubation with UCNLs. Even after 24 h at a high concentration of 1 mg/mL, more than 80% of the cells were still alive, indicating the low cytotoxity of the as-prepared UCNLs, which should be ascribed to the high biocompatibility of TaO_x shell [39–44].

Considering that UCNLs will be finally injected intravenously into blood vessels, it is necessary to guarantee the blood compatibility of these nanoparticles, such as low hemolytic effect. Herein, a hemolysis assay was preliminarily carried out based on the previous report [45]. As is shown in the inset (a) of the Fig. S9, there is no visible hemolysis effect for varied concentrations of UCNLs.

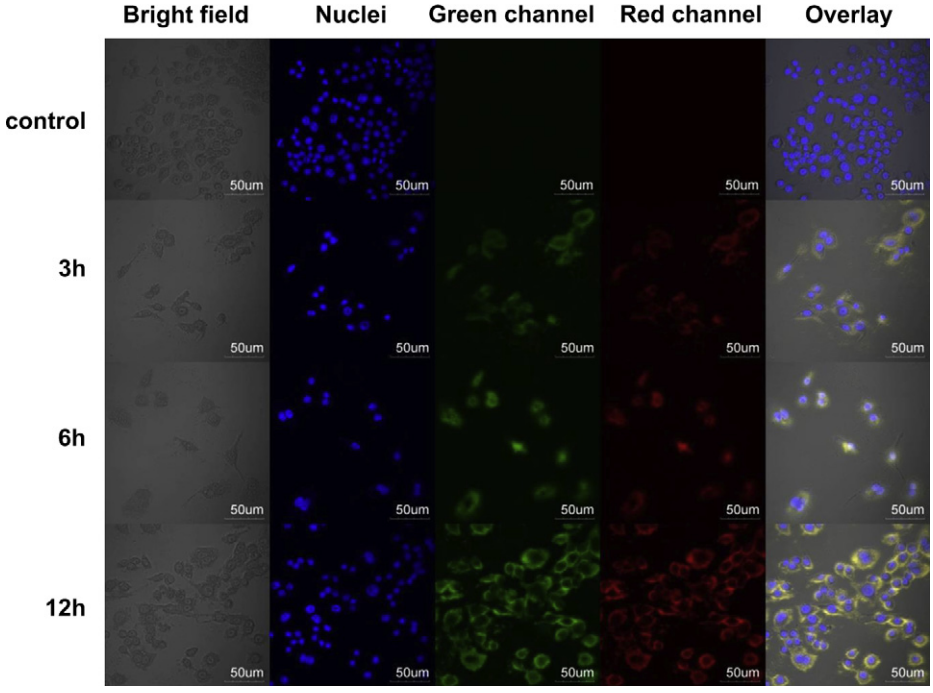

Fig. 4. Confocal fluorescence imaging of RAW264.7 cells incubated with UCNLs at 1000 μg/ml for different time durations of 3, 6 and 12 h.

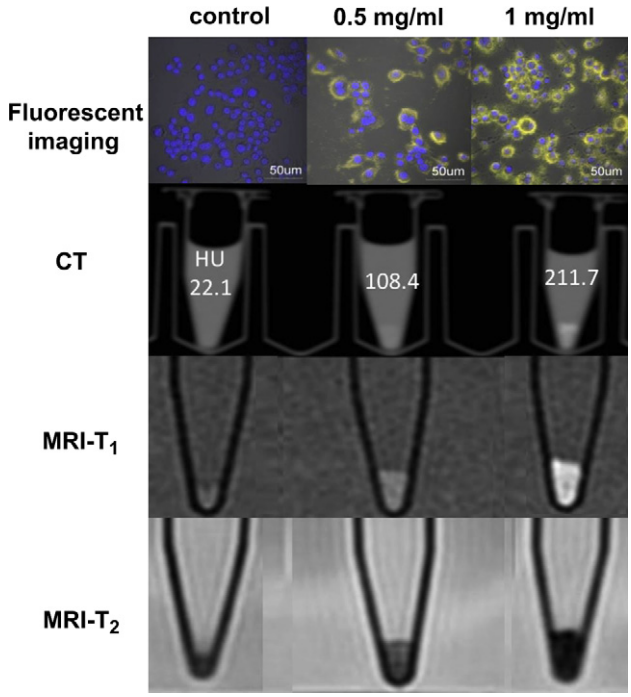

Fig. 5. Trimodal imaging results of RAW264.7 cells incubated with UCNL at concentrations of 0, 0.5 and 1 mg/mL. (a) Fluorescent imaging, (b) X-ray CT imaging of cell phantom (numbers indicate CT values in HU) and (c) T_1- and T_2-weighted MRI.

The exact RBC hemolyzed ratio was determined by measuring the absorbance of supernatants at 541 nm (hemoglobin) by UV–visible spectroscopy. Inset (b) in the Fig. S9 shows UV–Vis absorbance spectra of water (positive control), PBS (negative control) and UCNLs at the highest concentration (1 mg/mL) after interaction with RBCs. Only 2.9% hemolytic activity was present even at the concentration of up to 1 mg/mL, which decreased with the decline of the concentration (Fig. S9). The low and even negligible hemolytic activity should be originated from the outmost PEG shell serving as a protective layer and preventing the tantalum hydroxyl groups from access to RBCs [46].

3.4. Trimodal imaging of UCNL in vitro

The cellular uptake and trimodal imaging applicability of UCNLs were evaluated extensively *in vitro*. Cellular uptake experiments were conducted under the identical conditions by using a modified Olympus FV1000 laser-scanning confocal micro-scope (LSCM) equipped with a continuous wave (CW) NIR laser operating at $\lambda = 980$ nm. Fig. 4 reveals that the cellular uptake of UCNLs is a time-dependent process (sample concentration: 1 mg/mL), as demonstrated by gradually intensified intracellular luminescence at the prolonged incubations from 0 h to 12 h. In addition, *in vitro* trimodal images of RAW264.7 cells exposed to varied concentrations of the nanoparticles (0, 0.5 and 1 mg/mL) for 24 h are shown in Fig. 5, which demonstrates the gradually enhanced UCL/CT/MRI signal intensities as the concentration increased, indicating dose-dependent cellular uptakes of UCNLs and consequently effective trimodal imagings.

3.5. Trimodal imaging of UCNL in vivo

In vivo CT imaging of small animals revealed the bio-distribution of our probe at different time points (Fig. 6). The rapid accumulations of the probes in the liver and spleen were observed 10 min after injection, evidenced by the increased HU values (liver: from 64.6 to 95.5 and spleen: from 60.5 to 78), which implied that UCNLs entered the blood circulation and then were promptly phagocytosed by macrophages. The brightness enhancement in the same organs becomes more apparent at prolonged post-injection to 3 h, in accordance with the time-dependent HU values (Table S1). The long-lasting residence in the liver may facilitate the detection of hepatic metastases. In addition, it is well known that lymph node imaging is very essential for accurately detecting cancer metastases and improving cancer staging which are favorable for avoiding unnecessary surgery. Therefore, whether UCNL can enter lymph node was also examined by CT imaging of a mouse intradermally injected with UCNLs in the left forepaw. As seen in Fig. S10 and Mov. S1, there appears visually clear CT contrast enhancement in the axillary lymph node 2 h after injection, which demonstrates that UCNL could smoothly transfer to lymph nodes through lymphatic drainage and could be used as a CT contrast agent for possible lymph node mapping.

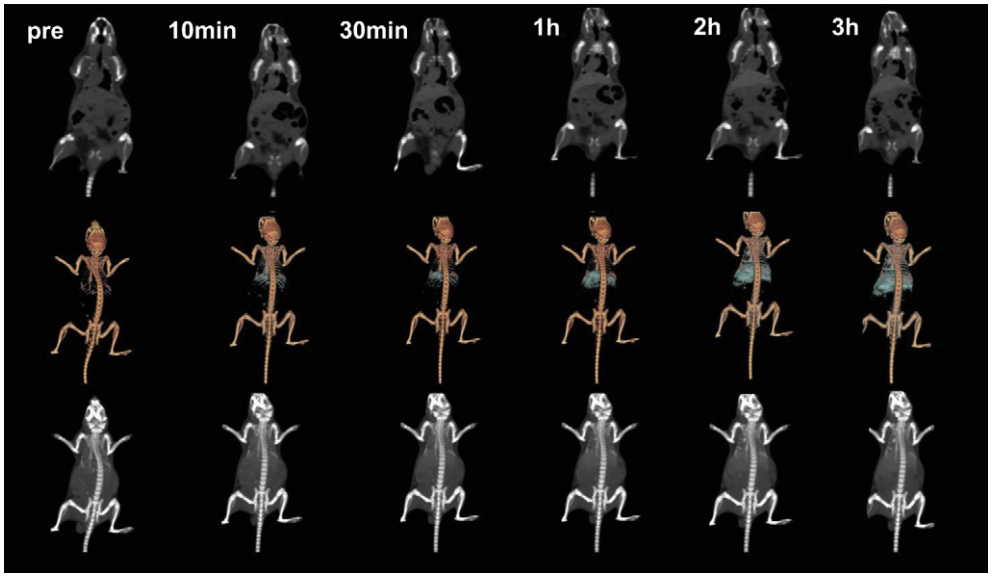

Fig. 6. *In vivo* X-ray CT imaging. Serial CT coronal views of a mouse at different time points after injecting UCNL solution (150 μL, 65 mg/mL) into the tail vein (top), the corresponding volume-rendered CT imaging (middle) and maximum intensity projections (bottom).

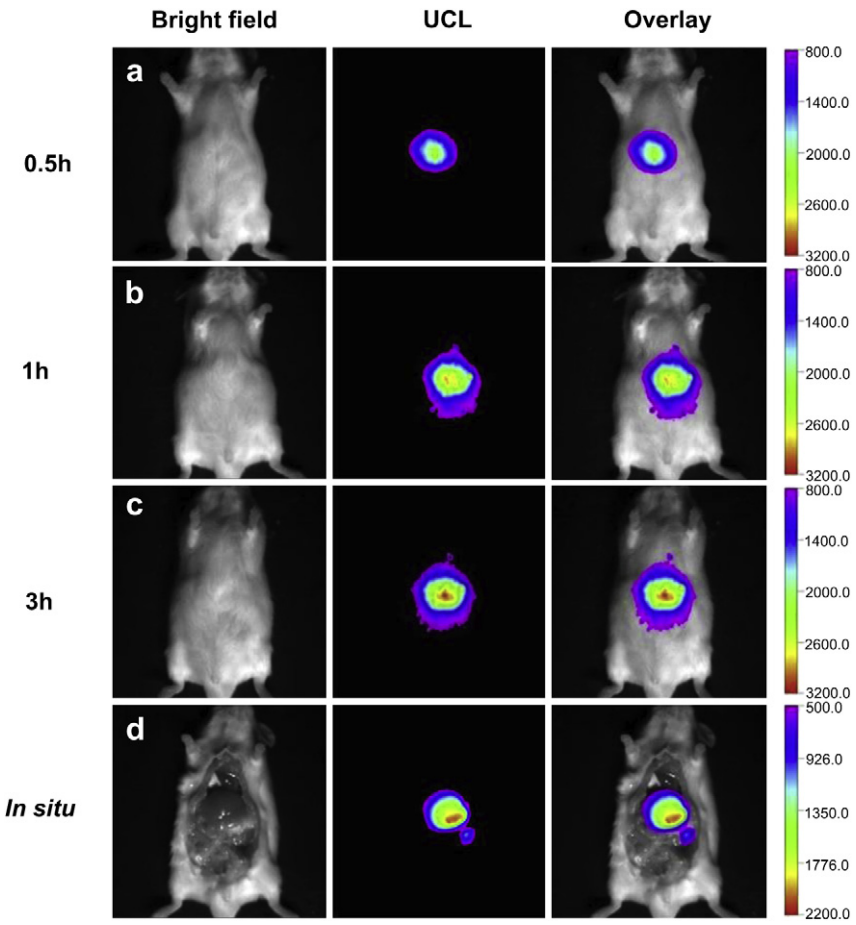

Fig. 7. *In vivo* UCL imaging after injection with UCNLs solutions (250 μL, 8 mg/mL) into a mouse at time points: 0.5 h (a), 1 h (b) and 3 h (c). The three images from the top were acquired under the same instrumental conditions (power density: 150 mW/cm^2 on the surface of the mouse). (d) *In situ* UCL imaging 3 h after injection acquired at power density of 50 mW/cm^2.

Supplementary video related to this article can be found at doi: 10.1016/j.biomaterials.2012.06.028.

To certify the feasibility of UCNLs as optical bioimaging nanoprobes *in vivo*, UCL imaging was performed on a mouse with UCNLs administrated through tail vein. The intense luminescence signal could be exclusively observed in liver and continuously enhanced with the increase of post-injection duration, which clearly indicated gradual elimination effect of reticuloendothelial system (RES)

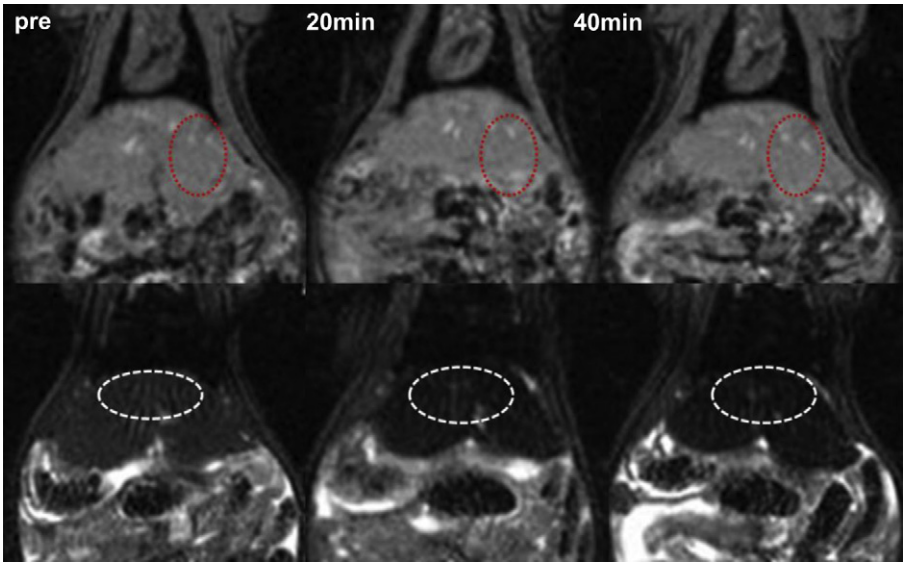

Fig. 8. *In vivo* coronal MR images of pre- and post-injection of UCNL solution for 20 and 40 min into a rat (Gd^{3+} contents: 647.5 μg/kg). Top: T_1-weighted images; Bottom: T_2-weighted images. The circled regions show the contrast enhancement in liver.

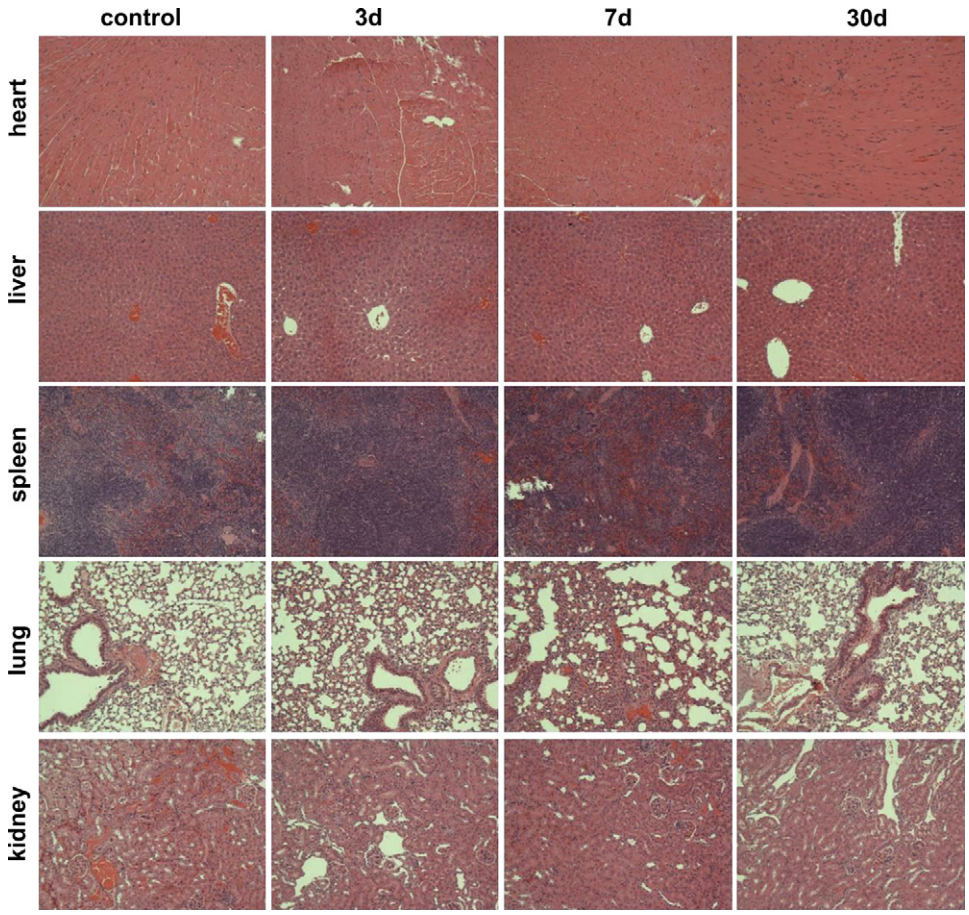

Fig. 9. H&E-stained tissue sections from mice to observe the time courses of the histological changes in liver, spleen, heart, kidney, and lung of mice receiving single intravenous injection of 150 μL of either PBS (control) or UCNL (65 mg/mL in PBS) followed by dissections in 3, 7 and 30 days post-injection.

serving as scavengers against foreign agents (Fig. 7a–c). Further bio-distribution investigation of UCNL, as presented by the *in situ* imaging of organs (Fig. 7d), revealed that the UCL signal originated predominately from the liver and spleen, whereas virtually no signal could be found in other organs without phagocytic cells. These results show that UCNL can be used for *in vivo* UCL imaging for organs/tissues that uptake UCNL.

The applicability of UCNLs as MRI contrast agents was examined *in vivo* by comparing MR images of pre- and post-injection of UCNLs on the whole body acquired on a 3.0 T MRI equipment. Fig. 8 shows detectable T_1- and remarkable T_2-weighted contrast enhancements in the liver area, as further evidenced by the changes of the signal intensities (Table S2). The positive and negative-contrast enhancement rates of signal intensities in liver were calculated to be 4.2% and −37.3% in 20 min post-injection and further increased to 5.3% and −50.2% in another 20min after injection (Fig. S11), suggesting the increased uptake of UCNLs by RES at the prolonged post-injection and the capability of simultaneous T_1- and T_2-weighted imagings *in vivo*.

3.6. Histology analysis of UCNL for small animals

Finally, histological changes were monitored by hematoxylin and eosin (H&E) staining at different time points (0, 3, 7 and 30 days) to study mid-term toxicity of these nanoparticles (Fig. 9). There were no significant evidences of tissue damage and adverse effect of the nanoparticles to various organs, which further confirmed the excellent biocompatibility of UCNLs.

4. Conclusion

A trimodal imaging nanoprobe has been constructed by decorating the radiopaque but fluorescence-transparent TaO_x onto the surface of $NaYF_4$:Yb^{3+}/Er^{3+}/Tm^{3+}@$NaGdF_4$ using a facile reverse microemulsion strategy. Such a nanoprobe exhibits excellent water-solubility and monodispersity with an average size of ~30 nm. High intensity/contrast CT/MRI/UCL trimodal imagings *in vitro* and *in vivo* could be achieved simultaneously without detectable imaging interference among the three modalities. The toxicity study demonstrated that UCNL barely had any significant harm to macrophage, RBCs and even biological tissue, reflecting its high biocompatibility. Based on these excellent performances, it is envisioned that by selecting another silane coupling agents and then linking appropriate targeted ligands, this material could be transformed into an excellent targeted trimodal imaging nanoprobe, which will be greatly favorable for precisely determining the location of lesions and decreasing the misdiagnosis in the early stage of diseases.

Acknowledgement

This work was financially supported by the National Natural Science Foundation of China Research (Grant No. 50823007, 50972154, 51132009, 51072212, 51102259, 21172043), the Science and Technology Commission of Shanghai (Grant No. 10430712800, 11nm0505000), the National Basic Research Program of China (973 Program, Grant No.2011CB707905). We thank Prof. Fuyou Li, Dr.

Yang Yang from Fudan University for the help in UCL *in vivo* imaging. We thank Jianan Liu, Wenpei Fan, Yu Chen, Lijun Wang, Jingwei Feng, Linlin Zhang and YanYang from Shanghai Institute of Ceramics, Chinese Academy of Sciences for useful discussions.

Appendix A. Supplementary data

Supplementary data related to this article can be found online at doi:10.1016/j.biomaterials.2012.06.028.

References

[1] Kalender WA. X-ray computed tomography. Phys Med Biol 2006;51:R29–43.
[2] Haller C, Hizoh I. The cytotoxicity of iodinated radiocontrast agents on renal cells in vitro. Invest Radiol 2004;39:149–54.
[3] Hizoh I, Haller C. Radiocontrast-induced renal tubular cell apoptosis-Hypertonic versus oxidative stress. Invest Radiol 2002;37:428–34.
[4] Rabin O, Manuel Perez J, Grimm J, Wojtkiewicz G, Weissleder R. An X-ray computed tomography imaging agent based on long-circulating bismuth sulphide nanoparticles. Nat Mater 2006;5:118–22.
[5] Oh MH, Lee N, Kim H, Park SP, Piao Y, Lee J, et al. Large-scale synthesis of bioinert tantalum oxide nanoparticles for X-ray computed tomography imaging and bimodal image-guided sentinel lymph node mapping. J Am Chem Soc 2011;133:5508–15.
[6] Bonitatibus JPJ, Torres AS, Goddard GD, FitzGerald PF, Kulkarni AM. Synthesis, characterization, and computed tomography imaging of a tantalum oxide nanoparticle imaging agent. Chem Commun 2010;46:8956–8.
[7] Kim D, Park S, Lee JH, Jeong YY, Jon S. Antibiofouling polymer-coated gold nanoparticles as a contrast agent for in vivo X-ray computed tomography imaging. J Am Chem Soc 2007;129:7661–5.
[8] Alric C, Taleb J, Duc GL, Mandon C, Billotey C, Meur-Herland AL, et al. Gadolinium chelate coated gold nanoparticles as contrast agents for both X-ray computed tomography and magnetic resonance imaging. J Am Chem Soc 2008;130:5908–15.
[9] Hainfeld JF, Slatkin DN, Focella TM, Smilowitz HM. Gold nanoparticles: a new X-ray contrast agent. Br J Radiol 2006;79:248–53.
[10] Popovtzer R, Agrawal A, Kotov NA, Popovtzer A, Balter J, Carey TE, et al. Targeted gold nanoparticles enable molecular CT imaging of cancer. Nano Lett 2008;8:4593–6.
[11] Kim Y-H, Jeon J, Hong SH, Rhim W-K, Lee Y-S, Youn H, et al. Tumor targeting and imaging using cyclic RGD-pegylated gold nanoparticle probes with directly conjugated iodine-125. Small 2011;7:2052–60.
[12] He M, Huang P, Zhang C, Hu H, Bao C, Gao G, et al. Dual phase-controlled synthesis of uniform lanthanide-doped $NaGdF_4$ upconversion nanocrystals via an OA/ionic liquid two-phase system for in vivo dual-modality imaging. Adv Funct Mater 2011;21:4470–7.
[13] Liu Y, Ai K, Liu J, Yuan Q, He Y, Lu L. A high-performance ytterbium-based nanoparticulate contrast agent for in vivo X-ray computed tomography imaging. Angew Chem Int Ed 2012;51:1437–42.
[14] Xing H, Bu W, Ren Q, Zheng X, Li M, Zhang S, et al. A $NaYbF_4$: Tm^{3+} nanoprobe for CT and NIR-to-NIR fluorescent bimodal imaging. Biomaterials 2012;33:5384–93.
[15] Zhu X, Zhou J, Chen M, Shi M, Feng W, Li F. Core–shell Fe_3O_4@$NaLuF_4$:Yb, Er/Tm nanostructure for MRI, CT and upconversion luminescence tri-modality imaging. Biomaterials 2012;33:4618–27.
[16] Matsuno H, Yokoyama A, Watari F, Uo M, Kawasaki T. Biocompatibility and osteogenesis of refractory metal implants, titanium, hafnium, niobium, tantalum and rhenium. Biomaterials 2001;22:1253–62.
[17] Black J. Biologic performance of tantalum. Clin Mater 1994;16:167–73.
[18] Findlay DM, Welldon K, Atkins GJ, Howie DW, Zannettino ACW, Bobyn D. The proliferation and phenotypic expression of human osteoblasts on tantalum metal. Biomaterials 2004;25:2215–27.
[19] Santra S, Yang H, Holloway PH, Stanley JT, Mericle RA. Synthesis of water-dispersible fluorescent, radio-opaque, and paramagnetic CdS: Mn/ZnS quantum dots: a multifunctional probe for bioimaging. J Am Chem Soc 2005;127:1656–7.
[20] Wang C, Tao H, Cheng L, Liu Z. Near-infrared light induced in vivo photodynamic therapy of cancer based on upconversion nanoparticles. Biomaterials 2011;32:6145–54.
[21] Yang T, Sun Y, Liu Q, Feng W, Yang P, Li F. Cubic sub-20 nm $NaLuF_4$-based upconversion nanophosphors for high-contrast bioimaging in different animal species. Biomaterials 2012;33:3733–42.
[22] Nyk M, Kumar R, Ohulchanskyy TY, Bergey EJ, Prasad PN. High contrast in vitro and in vivo photoluminescence bioimaging using near infrared to near infrared up-conversion in Tm^{3+} and Yb^{3+} doped fluoride nanophosphors. Nano Lett 2008;8:3834–8.
[23] Cao T, Yang Y, Gao Y, Zhou J, Li Z, Li F. High-quality water-soluble and surface-functionalized upconversion nanocrystals as luminescent probes for bioimaging. Biomaterials 2011;32:2959–68.
[24] Wang F, Han Y, Lim CS, Lu Y, Wang J, Xu J, et al. Simultaneous phase and size control of upconversion nanocrystals through lanthanide doping. Nature 2010;463:1061–5.
[25] Liu Q, Sun Y, Li C, Zhou J, Li C, Yang T, et al. ^{18}F-labeled magnetic-upconversion nanophosphors via rare-earth cation-assisted ligand assembly. ACS Nano 2011;5:3146–57.
[26] Zhou J, Sun Y, Du X, Xiong L, Hu H, Li F. Dual-modality in vivo imaging using rare-earth nanocrystals with near-infrared to near-infrared (NIR-to-NIR) upconversion luminescence and magnetic resonance properties. Biomaterials 2010;31:3287–95.
[27] Zhou J, Yu M, Sun Y, Zhang X, Zhu X, Wu Z, et al. Fluorine-18-labeled Gd^{3+}/Yb^{3+}/Er^{3+} co-doped $NaYF_4$ nanophosphors for multimodality PET/MR/UCL imaging. Biomaterials 2011;32:1148–56.
[28] Xing H, Bu W, Zhang S, Zheng X, Li M, Chen F, et al. Multifunctional nanoprobes for upconversion fluorescence, MR and CT trimodal imaging. Biomaterials 2012;33:1079–89.
[29] Chen F, Bu W, Zhang S, Liu X, Liu J, Xing H, et al. Positive and negative lattice shielding effects co-existing in Gd (III) ion doped bifunctional upconversion nanoprobes. Adv Funct Mater 2011;21:4285–94.
[30] Hu H, Xiong L, Zhou J, Li F, Cao T, Huang C. Multimodal-luminescence core–shell nanocomposites for targeted imaging of tumor cells. Chem Eur J 2009;15:3577–84.
[31] Zhang T, Ge J, Hu Y, Yin Y. A general approach for transferring hydrophobic nanocrystals into water. Nano Lett 2007;7:3203–7.
[32] Sun Y, Sermon PA, Vong MSW. Design of reflective tantala optical coatings using sol-gel chemistry with ethanoic acid catalyst and chelator. Thin Solid Films 1996;278:135–9.
[33] Xia A, Gao Y, Zhou J, Li C, Yang T, Wu D, et al. Core-shell $NaYF_4$:Yb^{3+}, Tm^{3+}@Fe_xO_y nanocrystals for dual-modality T_2-enhanced magnetic resonance and NIR-to-NIR upconversion luminescent imaging of small-animal lymphatic node. Biomaterials 2011;32:7200–8.
[34] Alvarez-Lorenzo C, Bromberg L, Concheiro A. Light-sensitive intelligent drug delivery systems. Photochem Photobiol 2009;85:848–60.
[35] Zhang G, Liu Y, Yuan Q, Zong C, Liu J, Lu L. Dual modal in vivo imaging using upconversion luminescence and enhanced computed tomography properties. Nanoscale 2011;3:4365–71.
[36] Kumar R, Nyk M, Ohulchanskyy TY, Flask CA, Prasad PN. Combined optical and MR bioimaging using rare earth ion doped $NaYF_4$ nanocrystals. Adv Funct Mater 2009;19:853–9.
[37] Guo H, Li Z, Qian H, Hu Y, Muhammad IN. Seed-mediated synthesis of $NaYF_4$:Yb, Er/$NaGdF_4$ nanocrystals with improved upconversion fluorescence and MR relaxivity. Nanotechnology 2010;21:125602.
[38] Johnson NJJ, Oakden W, Stanisz GJ, Prosser RS, van Veggel FCJM. Size-tunable, ultrasmall $NaGdF_4$ nanoparticles: insights into their T_1 MRI contrast enhancement. Chem Mater 2011;23:3714–22.
[39] Kato H, Nakamura T, Nishiguchi S, Matsusue Y, Kobayashi M, Miyazaki T, et al. Bonding of alkali- and heat-treated tantalum implants to bone. J Biomed Mater Res 2000;53:28–35.
[40] Sagomonyants KB, Hakim-Zargar M, Jhaveri A, Aronow MS, Gronowicz G. Porous tantalum stimulates the proliferation and osteogenesis of osteoblasts from elderly female patients. J Orthop Res 2011;29:609–16.
[41] Sharma CP, Paul W. Protein-interaction with tantalum – changes with oxide layer and hydroxyapatite at the interface. J Biomed Mater Res 1992;26:1179–84.
[42] Shtansky DV, Gloushankova NA, Bashkova IA, Kharitonova MA, Moizhess TG, Sheveiko AN, et al. Ta-doped multifunctional bioactive nanostructured films. Surf Coat Technol 2008;202:3615–24.
[43] Balla VK, Bose S, Davies NM, Bandyopadhyay A. Tantalum-a bioactive metal for implants. JOM 2010;62:61–4.
[44] Blanco JF, Sanchez-Guijo FM, Carrancio S, Muntion S, Garcia-Brinon J, del Canizo MC. Titanium and tantalum as mesenchymal stem cell scaffolds for spinal fusion: an in vitro comparative study. Eur Spine J 2011;20:353–60.
[45] Slowing II, Wu CW, Vivero-Escoto JL, Lin VSY. Mesoporous silica nanoparticles for reducing hemolytic activity towards mammalian red blood cells. Small 2009;5:57–62.
[46] Lin Y-S, Haynes CL. Impacts of mesoporous silica nanoparticle size, pore ordering, and pore integrity on hemolytic activity. J Am Chem Soc 2010;132:4834–42.